






Magnetism in the axion insulator candidate $\text{Eu}_5\text{In}_2\text{Sb}_6$

M. C. Rahn ^{1,2,*} M. N. Wilson,^{3,4} T. J. Hicken ^{3,5} F. L. Pratt,⁶ C. Wang,⁵ F. Orlandi ⁶ D. D. Khalyavin,⁶ P. Manuel,⁶ L. S. I. Veiga,^{7,8} A. Bombardi,⁸ S. Francoual ⁹ P. Bereciartua,⁹ A. S. Sukhanov,¹ J. D. Thompson,² S. M. Thomas,² P. F. S. Rosa,² T. Lancaster ³ F. Ronning,² and M. Janoschek^{2,10,11,†}

¹*Institute for Solid State and Materials Physics, Technical University of Dresden, 01062 Dresden, Germany*

²*Los Alamos National Laboratory, Los Alamos, New Mexico 87545, USA*

³*Department of Physics, Durham University, South Road, Durham, DH1 3LE, United Kingdom*

⁴*Memorial University, Department of Physics and Physical Oceanography, St. John's, NL, A1B 3X7, Canada*

⁵*Laboratory for Muon-Spin Spectroscopy, Paul Scherrer Institute, CH-5232 Villigen, Switzerland*

⁶*ISIS Facility, STFC, Rutherford Appleton Laboratory, Chilton, Didcot, Oxfordshire, OX11 0QX, United Kingdom*

⁷*London Centre for Nanotechnology and Department of Physics and Astronomy,*

University College London, London WC1E 6BT, United Kingdom

⁸*Diamond Light Source Ltd., Didcot OX11 0DE, United Kingdom*

⁹*Deutsches Elektronen-Synchrotron (DESY), Hamburg, Germany*

¹⁰*Laboratory for Neutron and Muon Instrumentation, Paul Scherrer Institute, CH-5232 Villigen, Switzerland*

¹¹*Physik-Institut, Universität Zürich, CH-8057 Zürich, Switzerland*



(Received 28 December 2023; revised 4 March 2024; accepted 18 March 2024; published 2 May 2024)

$\text{Eu}_5\text{In}_2\text{Sb}_6$ is a member of a family of orthorhombic nonsymmorphic rare-earth intermetallics that combines large localized magnetic moments and itinerant exchange with a low carrier density and perpendicular glide planes. This may result in special topological crystalline (wallpaper fermion) or axion insulating phases. Recent studies of $\text{Eu}_5\text{In}_2\text{Sb}_6$ single crystals have revealed colossal negative magnetoresistance and multiple magnetic phase transitions. Here, we clarify this ordering process using neutron scattering, resonant elastic x-ray scattering, muon spin-rotation, and magnetometry. The nonsymmorphic and multisite character of $\text{Eu}_5\text{In}_2\text{Sb}_6$ results in coplanar noncollinear magnetic structures with an Ising-like net magnetization along the a axis. A reordering transition, attributable to competing ferro- and antiferromagnetic couplings, manifests as the onset of a second commensurate Fourier component. In the absence of spatially resolved probes, the experimental evidence for this low-temperature state can be interpreted either as an unusual double- q structure or in a phase separation scenario. The net magnetization produces variable anisotropic hysteretic effects which also couple to charge transport. The implied potential for functional domain physics and topological transport suggests that this structural family may be a promising platform to implement concepts of topological antiferromagnetic spintronics.

DOI: [10.1103/PhysRevB.109.174404](https://doi.org/10.1103/PhysRevB.109.174404)

I. INTRODUCTION

The guided design and control of topologically protected conduction states on surfaces and interfaces of bulk insulators and semimetals is one of the most sought-after results of quantum materials physics. The concept of topological quantum chemistry [1] has enabled high-throughput calculations and predictions of topological band properties in the absence of electronic correlations [2,3]. While progress on intrinsically magnetic topological matter has been much slower, the

analysis of all magnetic space groups and tabulated magnetic structures indicates that there is indeed an abundance of candidate strongly correlated materials with potential for functional band-topology [4,5]. However, as magnetic symmetry cannot currently be predicted from first principles, the identification of suitable material platforms remains an outstanding challenge.

Following the proposal of fourfold degenerate Dirac surface states with hourglass connectivity in the nonsymmorphic orthorhombic Zintl phase $\text{Ba}_5\text{In}_2\text{Sb}_6$ [6], there has been increased interest in magnetic members of this 5-2-6 structural family. The narrow band-gap semiconductor $\text{Eu}_5\text{In}_2\text{Sb}_6$ has been previously studied for its outstanding thermoelectric properties at high temperature [7,8]. Following the synthesis of single-crystalline samples, the material revealed highly unusual low-temperature properties, including colossal magnetoresistance, which has been attributed to the localization of charge carriers at magnetic polarons [9–11]. In-depth density functional studies of Eu-based 5-2-6 compounds have

*marein.rahn@tu-dresden.de

†marc.janoschek@psi.ch

since identified the potential for axion insulating phases and predicted a high sensitivity to chemical and pressure/strain tuning [12]. However, both the electronic and magnetic structures of the 5-2-6 compounds have so far eluded experimental determination.

Here, we report on the complex magnetic ordering process of $\text{Eu}_5\text{In}_2\text{Sb}_6$. Using muon spin-rotation (μSR), neutron powder diffraction, and resonant elastic x-ray scattering (REXS), we are able to shed light on an unusual two-step ordering process due to the nonsymmorphic and multisite character of $\text{Eu}_5\text{In}_2\text{Sb}_6$. Unexpectedly, our findings imply the existence of net-magnetized domains, and angle-dependent electrical resistivity measurements indicate coupling of magnetism and charge transport.

Figure 1(a) illustrates the orthorhombic $Pbam$ unit cell of $\text{Eu}_5\text{In}_2\text{Sb}_6$. The structure can be understood as layers of coplanar Eu ions (ten per unit cell) that are interpenetrated by chains of corner-sharing InSb_4 tetrahedra along the c axis. The figure also illustrates the positions of the b glide (blue), the a glide (red), and the mirror plane (gray). The perpendicular glide planes endow the Eu layers with the symmetry of the wallpaper group pgg , encountered in daily life as the herringbone pattern [13]. This combination of nonsymmorphic symmetries is the prerequisite for the topological-crystalline phases predicted in this structural family [6]. In $\text{Eu}_5\text{M}_2\text{X}_6$ compounds [12], this potential for nontrivial topology combines with the large magnetic moment of divalent europium ($S = 7/2$, $L = 0$, $\mu \approx 8\mu_B$).

We find that below the Néel temperature $T_N = 14.5$ K, the Eu^{2+} spins initially form a complex coplanar, noncollinear arrangement (Γ) that carries a net magnetic moment along the a axis, as illustrated in Fig. 1(b). Below $T_Z = 7.5$ K, this phase is either gradually displaced by a growing volume fraction of another magnetic phase (Z) or it forms a double- q state with perpendicular Γ and Z components. Crucially, the per-layer spin arrangements of the Γ and Z components obey the same magnetic symmetries—they differ only in the (parallel vs. alternating) stacking of this motif along the c axis. While all three magnetic states (Γ , Z , double- q) conserve inversion symmetry \mathcal{I} , effective time-reversal symmetry $\{\mathcal{T}|00\frac{1}{2}\}$ is only conserved in the Z state, which would make these regions candidate axion insulators [14,15]. The phase separation scenario could therefore provide a platform to explore interfaces of topologically distinct insulating regimes.

II. RESULTS AND INTERPRETATION

Previous measurements of the heat capacity and magnetic susceptibility [9], reproduced in Figs. 2(c) and 2(d), revealed two continuous magnetic transitions, which correspond to the Néel temperature $T_N = 14.5$ K and the onset of the Z component at $T_Z = 7.5$ K. The magnetic neutron powder diffraction patterns in Fig. 2(a) illustrate that magnetic Bragg peaks in the intermediate phase ($T_Z < 10 \text{ K} < T_N$) can be indexed by the propagation vector $\mathbf{q}_\Gamma = (0, 0, 0)$. The low-temperature data set ($1.5 \text{ K} < T_Z$) features both \mathbf{q}_Γ and $\mathbf{q}_Z = (0, 0, 1/2)$ peaks [13].

Using REXS at the Eu L edges, we characterized the \mathbf{q}_Z and \mathbf{q}_Γ magnetic order in more detail. Figure 2(b) shows the thermal evolution of Bragg intensities associated with the two

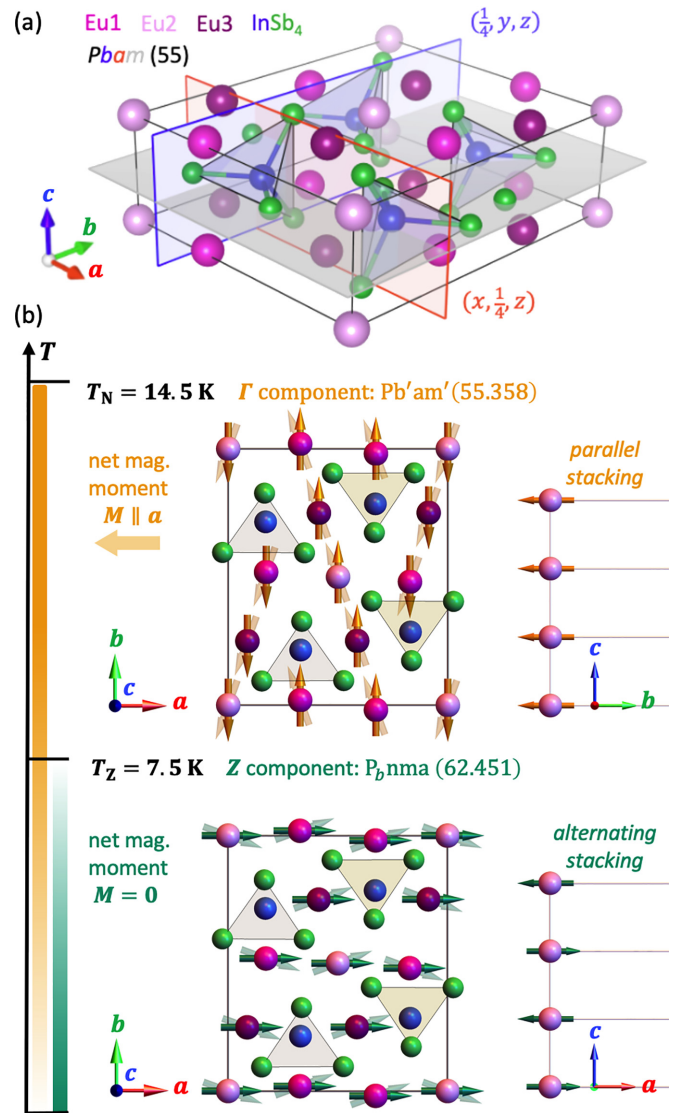


FIG. 1. (a) The orthorhombic unit cell and $Pbam$ symmetries of $\text{Eu}_5\text{In}_2\text{Sb}_6$. The perpendicular glide planes are highlighted in blue and red. (b) Solid arrows show the spin arrangement inferred for the Γ magnetic component, which forms at $T_N = 14.5$ K. The structure is collinear within the uncertainty of the neutron diffraction data. Shaded arrows illustrate tilts away from this collinear configuration, which creates a net magnetization. (c) Corresponding views of the Z magnetic component, which originates below $T_Z = 7.5$ K. The x-ray and neutron scattering data do not allow the distinction between a double- q state and magnetic phase separation. Both Γ and Z components are described by the same magnetic basis vectors, which generally add to a per-layer magnetization along the a axis. For the Γ component, this results in a spontaneous macroscopic magnetization, while in the Z component it is compensated by alternating stacking.

Fourier components. These intensities are not necessarily a direct measure of the ordered magnetic moment because the magnetic order has degrees of freedom that affect the structure factor and may evolve with temperature. Nevertheless, the rise of \mathbf{q}_Z intensity below T_Z appears to be proportional to the reduction of the \mathbf{q}_Γ peak, consistent with the displacement of the Γ by the Z -type Fourier component. While for a double- q

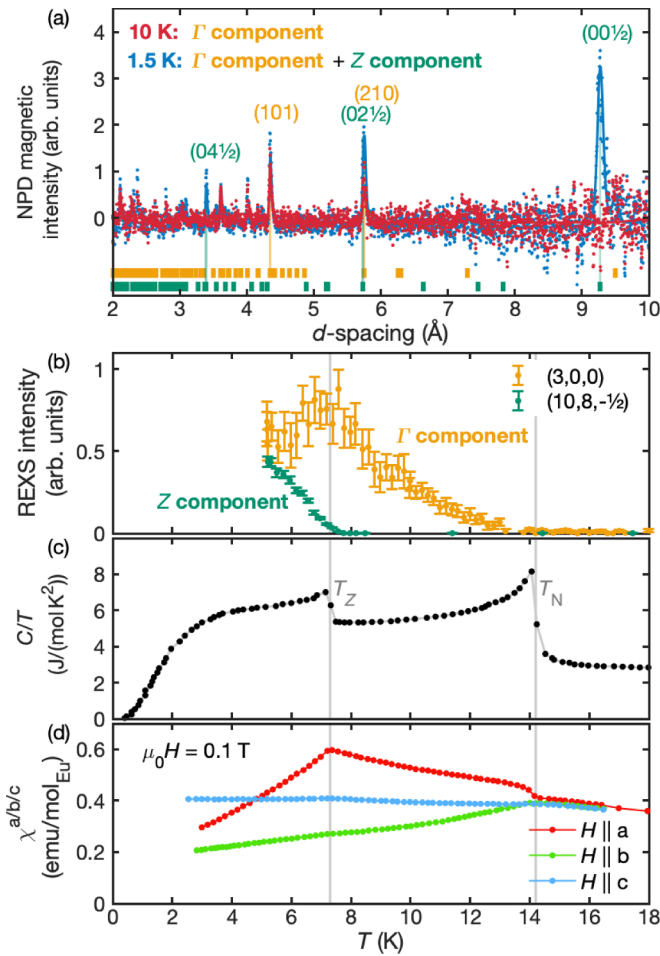


FIG. 2. (a) Magnetic neutron powder diffraction at 1.5 K and 10 K. The nuclear intensity (at 25 K) has been subtracted from the data [13]. (b) Temperature dependence of REXS intensities associated with the propagation vectors of the Ising weakly ferromagnetic Γ order and the compensated antiferromagnetic Z component. Below $T_Z = 7.5$ K, Γ and Z either coexist by phase separation or as a double- q structure. (c) The consecutive second-order phase transitions at 14.5 K and 7.5 K observed in heat capacity (C/T). (d) The anisotropic magnetic susceptibility $\chi^{a/b/c}(T)$ at 100 mT applied along the principal axes. Note the small spontaneous magnetization of χ^a in the Γ state and the change in easy axis below T_Z .

model the Γ/Z ratio may be different at each Wyckoff site, the refinement of the 1.5 K neutron powder diffraction data in the phase separation scenario results in phase volumes of 34% (Z) and 66% (Γ) [13].

Azimuthal scans and full linear polarization analysis of the REXS signal, shown in the Supplemental Material [13], reveal the direction of magnetic structure factor vectors of individual Bragg peaks. Combined with representational analysis, this information determines the irreducible representations (irreps) associated with the two magnetic phases [13]. The Γ and Z magnetic structures are described by the irreps Γ_3^+ ($Pb'am'$) and Z_3^+ ($P_b nma$), and the superposition of both would correspond to magnetic space group $Pb'am'$. Crucially, these two irreps impose the same phase relations (basis vectors) on the relative alignment of the coplanar magnetic moments—the two magnetic components differ only in the parallel (Γ) or

alternating (Z) stacking of this motif along the c axis. Given that magnetometry reveals a localized $S = 7/2$ ($\approx 8 \mu_B$) [9], a physical model should require the same magnitude of the magnetic moments in each layer. Cancellation of the Γ/Z magnetic basis vectors in every second layer can be avoided under the special condition that the Fourier components associated with either irrep must be perpendicular to one another. An illustration of the resulting type of double- q order is given in the Supplemental Material [13].

As indicated by solid arrows in Figs. 1(b) and 1(c), we find that the magnetic components associated with the Γ and Z magnetic structures are close to collinear with the b and a axes, respectively. The shaded arrows illustrate tilts away from the collinear structures that are allowed by symmetry and evidenced by magnetometry. The magnitude of the tilts is either smaller than the uncertainty of the data (neutron scattering) or $1^\circ \sim 10^\circ$ (REXS, Z component).

The per-layer arrangement of the ten magnetic moments has several important implications. The Eu ions occupy one twofold and two fourfold Wyckoff sites, as indicated by different shades in Fig. 1 (see Ref. [13] for more detailed illustrations). The overall structure is defined by three in-plane spin orientations (one per site), which may vary continuously with temperature. Crucially, the components of the magnetic moments (anti)parallel to the b axis cancel necessarily, but all a -axis components per Wyckoff orbit are parallel. Given the 2/4/4 multiplicity, they can, therefore, in general, not be compensated between the three sites. This makes each layer a weak (canted) Ising ferromagnet with a variable net magnetization along the a axis. Notably, this holds true independently of whether the moments are mostly aligned with the a or b axis, as shown in Fig. 1(b). For instance, in the Γ component, the net magnetization of layers is small because the moments are, within the accuracy of our measurements, aligned with the b axis. However, small tilts away from this collinear configuration (indicated by shaded arrows) produce a small net moment along a , which adds up to a macroscopic magnetization. Conversely, the Z magnetic component carries a large per-layer magnetization along a (the spins are close to collinear along a), but here this is compensated by the alternating stacking.

Knowledge of this magnetic order explains several unusual observations of bulk and local magnetic probes. For example, in Fig. 2(d), the $H \parallel a$ magnetic susceptibility $\chi^a(T)$ shows a ferromagnet-like increase below T_N . This is not compatible with conventional antiferromagnetism but can now be explained by the weak $M \parallel a$ ferromagnetism. Below T_Z , the bulk susceptibility gradually takes on the character of the Z magnetic structure shown in Fig. 1(b): As the weakly ferromagnetic (Γ) component recedes, $\chi^a(T)$ decreases rapidly. Eventually (below ≈ 5 K), the magnetic susceptibility is largest for $H \parallel c$, as expected of a coplanar antiferromagnet. Given that the moments of the Z component align largely with the a axis, see Fig. 1(b), χ^a should be minimal once the Z component dominates. Accordingly, the gradient of $\chi^a(T)$ below T_Z is much steeper than that of $\chi^b(T)$.

To probe the magnetic ordering process from a local point of view, we turn to muon spin-rotation (μ SR) experiments. To reveal both static and dynamic characteristics (μ s timescale), we measured spectra at continuous (PSI/GPS) and

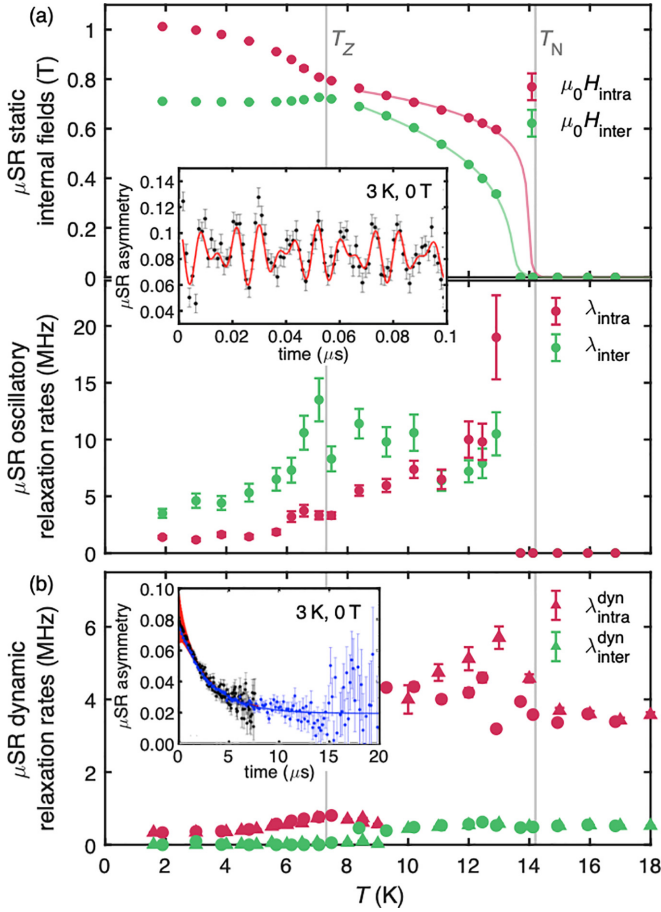


FIG. 3. (a) Static internal fields (top) and corresponding relaxation rates (bottom) determined by zero-field continuous-source μ SR (GPS instrument). Solid lines are a guide to the eye. We attribute different components of the μ SR asymmetry to muon stopping sites that are more sensitive to fields within (intra) and between (inter) the layers. The inset shows an example of the μ SR asymmetry measured at GPS (3 K, typical fit indicated by a red line). (b) Dynamic relaxation rates determined from the decay of the zero-field μ SR asymmetry up to 20 μ s. Circles and triangles mark values inferred from data measured at continuous (GPS) and pulsed source (EMU) muon instruments, respectively. The inset shows a typical fit in this time window, including both continuous source (black) and pulsed source data (blue).

pulsed (ISIS/EMU) muon sources. The observed μ SR asymmetry can be interpreted by assuming two types of muon stopping sites. Each contributes an oscillatory component associated with a characteristic relaxation rate λ and a dynamical relaxation λ^{dyn} (due to fluctuating fields). One possible interpretation of the fit results is that one class of stopping site is more sensitive to magnetic fields within the planes (intra) and the other is more sensitive to fields between the planes (inter). The variation of these characteristics throughout the ordering process, along with exemplary fits to the data, is shown in Fig. 3.

As seen in Fig. 3(a), the oscillatory signal that we associate with quasistatic in-plane fields H_{intra} sets in abruptly at T_N , as often observed for materials with two-dimensional correlations. By contrast, the gradual onset of H_{inter} is more typical

for three-dimensional magnetism. Interestingly, as seen in Fig. 3(b), neither dynamical relaxation $\lambda_{\text{inter}}^{\text{dyn}}$, nor $\lambda_{\text{intra}}^{\text{dyn}}$, which encode magnetic fluctuations, have strong anomalies at T_N . The transition could therefore be interpreted as a freezing-out of preexisting short-range magnetic correlations.

At T_Z , the absence of discontinuities of the static fields in Fig. 3(a) is consistent with the picture that the local magnetic structure does not change abruptly. Since the onset of an alternating stacking (Z) component does not affect the per-layer magnetic symmetry, the static fields within the layers (H_{intra} , λ_{intra}) are not strongly affected by this transition. By contrast, the onset of the Z component qualitatively changes the trend of H_{inter} and causes an anomaly in λ_{inter} . Moreover, as shown in Fig. 3(b), both dynamic relaxation rates ($\lambda_{\text{inter}}^{\text{dyn}}$, $\lambda_{\text{intra}}^{\text{dyn}}$) collapse around T_Z . This implies that the magnetism overall becomes much more static, possibly because competition between magnetic correlations is relieved. Below T_Z , H_{inter} has a slight tendency to decrease upon cooling. This unusual behavior may reflect changes in the domain structure, as previously suggested in GaV_4S_8 [16,17]. Notably, the relative amplitudes of the components do not change below T_Z , as one might expect for varying volume fractions. Although this might be taken as evidence for the double- q scenario, the nature of the Γ and Z magnetic orders (which share the same magnetic symmetry per layer) means that we cannot discount the phase separation picture.

Neither local nor bulk magnetic probes nor magnetic scattering allow a clear distinction between a double- q or phase separation scenario below T_Z . In either case, the net magnetization of the Γ state implies that Ising-like magnetic domains and their interplay on the mesoscale may play an important role in $\text{Eu}_5\text{In}_2\text{Sb}_6$, as illustrated in Fig. 4. For instance, as observed in other phase-separated magnets [18], interfaces of ferromagnetic domains may provide natural nucleation points for the growth of antiferromagnetic (Z) regimes. As illustrated in Figs. 4(a) and 4(b), Γ domains with an odd number of layers could be converted entirely into a Z region. By contrast, Γ domains with an even number of layers necessarily leave behind antiferromagnetic domain walls with net magnetization [19]. Even if the Z fraction should approach 100%, the magnetization would not be fully compensated and the magnetic state would not be homogeneous. This scenario could explain that even at low T , predominantly Z magnetic states would feature spontaneous magnetization and hysteretic effects.

Domain effects provide a compelling scenario to understand the unusual field cooled and zero-field cooled (FC/ZFC) characteristics of the $H \parallel a$ magnetic susceptibility shown in Fig. 4(c). Upon warming, a ZFC sample in which, at low T , the opposite domain configuration happens to be encoded shows the same (FC) magnetic susceptibility curve of opposite sign until the thermal energy is sufficient to allow consecutive flips of Γ domains (or domains carrying a Γ component) into the field direction. The observed sign reversal of the magnetic susceptibility might be attributable to a specific Γ -component domain structure dictated by demagnetization fields (which would be compatible both the phase separation and double- q scenarios). Details of this process should depend on the sample shape or pinning centres of antiferromagnetic domain walls, which could be verified by imaging techniques.

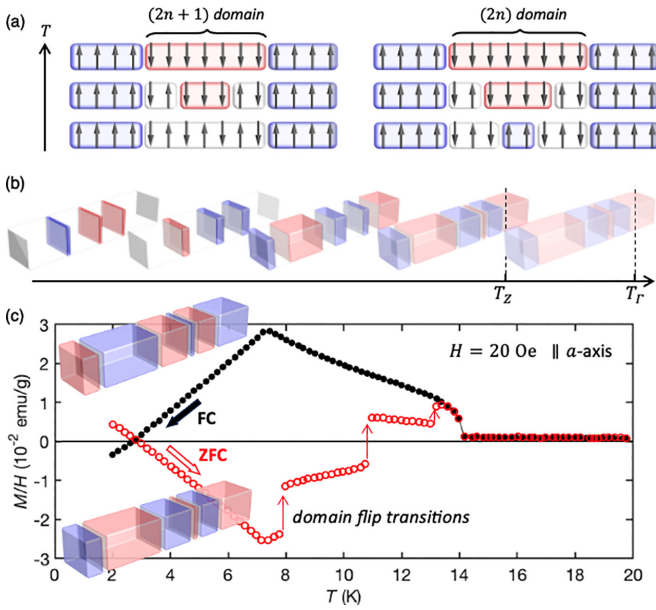


FIG. 4. (a) Illustration of the magnetic phase separation scenario below T_Z . Each layer of $\text{Eu}_5\text{In}_2\text{Sb}_6$ is represented by an arrow indicating the direction of the Ising (per-layer) net magnetic moment. Up (down) domains of the \mathbf{q}_T state are colored blue (red). Interfaces between Γ domains may provide natural nucleation points of the Z state (white). Γ domains with an even ($2n$) number of layers prevent the formation of a homogeneous Z ordered state. They leave behind antiferromagnetic domain walls that carry a net magnetic moment and could also contribute to hysteretic effects. (b) Sketch of the thermal evolution of an $\text{Eu}_5\text{In}_2\text{Sb}_6$ slab, colored in analogy to (a). (c) Field-cooled and zero-field cooled (FC/ZFC) curves of the magnetic susceptibility measured with a weak (20 Oe) bias field along the a axis. Magnetization reversal and domain flip transitions [indicated by inset illustrations] provide a tentative explanation for these unusual characteristics.

The magnetism of $\text{Eu}_5\text{In}_2\text{Sb}_6$ appears to be coupled to charge transport over a wide temperature range. Figure 5(a) illustrates that the μSR dynamic relaxation rates $\lambda_{\text{intra}}^{\text{dyn}}$ and $\lambda_{\text{inter}}^{\text{dyn}}$, associated with slow magnetic dynamics, increase significantly when cooling below $T^* \approx 35$ K. This temperature scale has previously been associated with the onset of strong short-ranged antiferromagnetic correlations [9]. As illustrated in Fig. 5(b), T^* also coincides with the temperature below which the resistance diverges from activated behavior, $R \propto T \exp(42 \text{ meV}/k_B T)$ [9]. Taken together, this suggests that below T^* , the charge transport in $\text{Eu}_5\text{In}_2\text{Sb}_6$ starts being affected by magnetic dynamics.

Hysteretic characteristics in $\text{Eu}_5\text{In}_2\text{Sb}_6$ change throughout the magnetic ordering process, with a variable effect on charge transport. As illustrated in Fig. 5(c), we identify three temperature regimes of charge transport: The CMR regime above $T > 10.5$ K (III), the region $3.0 \text{ K} < T < 10.5$ K where the resistance is reduced by more than five orders of magnitude (II), and a steep rise of resistance below $T < 3.5$ K (I). Figures 6(a)–6(d) show how the resistance (current $I \parallel \hat{c}$) varies under an azimuthal rotation in an applied field of 1 T. The three transport regimes differ not only quantitatively (in the magnitude of R) but also qualitatively.

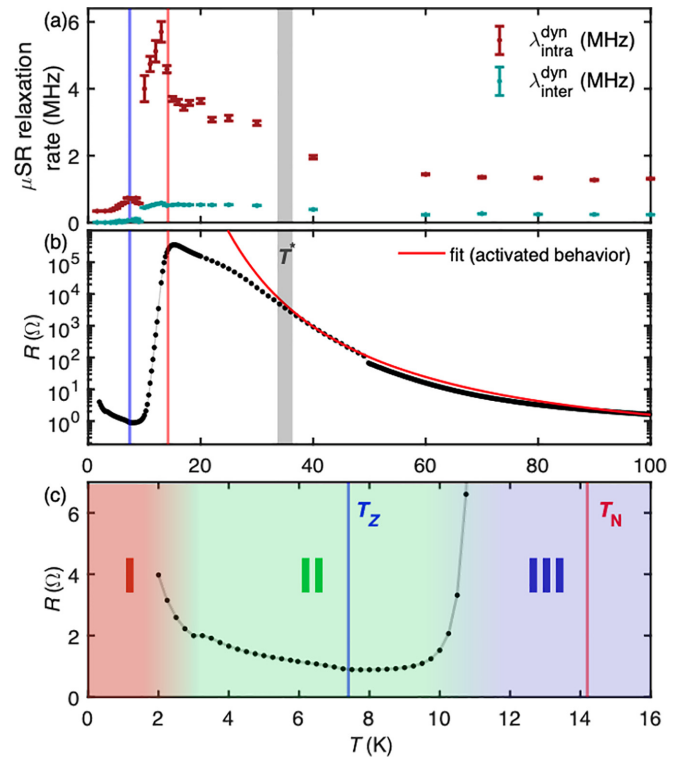


FIG. 5. (a) Pulsed-source μSR measurements of the dynamic relaxation rates $\lambda_{\text{intra}}^{\text{dyn}}$ and $\lambda_{\text{inter}}^{\text{dyn}}$ indicate an onset of short-ranged magnetic correlations at $T^* \approx 35$ K. This is consistent with the interpretation in terms of interacting magnetic polarons proposed in Ref. [9]. (b) On the same temperature scale, the resistance R (current $I \parallel c$, log scale) begins to diverge from activated behavior. (c) Detailed view of the resistance within the magnetically ordered phase (linear scale). We identify three regimes of charge transport (I, II, III).

The corresponding Figs. 6(e)–6(l) show hysteretic effects for fields applied along the a and b axes, as observed in the magnetization Figs. 6(e)–6(h) and resistance Figs. 6(i)–6(l). To isolate the hysteretic components ΔM and ΔR , a linear slope was subtracted from the $M(H)$ curves, and up and down ramps of $R(H)$ were subtracted (for reference, we show the raw data in the Supplemental Material [13]). The observations are similar at 5 K and 10 K (i.e., below and above T_Z); see Figs. 6(f) and 6(g) and Figs. 6(j) and 6(k). Specifically, both ΔM and ΔR are negligible for $H \parallel \hat{b}$, but sizable and of coinciding coercive fields for $H \parallel \hat{a}$. This matches the expectations for the reversal of weakly ferromagnetic domains, which are indeed expected below and above T_Z . Variations of the coercive field and remanent magnetization between 5 K and 10 K are expected, given the trade-off between a decreasing ordered magnetic moment and an increasing Γ Fourier component, or possibly Γ volume fraction. The linear $\Delta R(H) \propto \pm H$ at low temperatures distinguishes the hysteretic effects in regimes (I, II) against the much larger and nonmonotonic $\Delta R(H)$ in the CMR regime (III). Interestingly, $\Delta R(H)$ changes signs between (I) and (II), but retains its association with the a axis. As bulk and transport measurements are not sensitive to the spatial distribution of the spontaneous magnetization, they do not allow us to distinguish between the phase separation

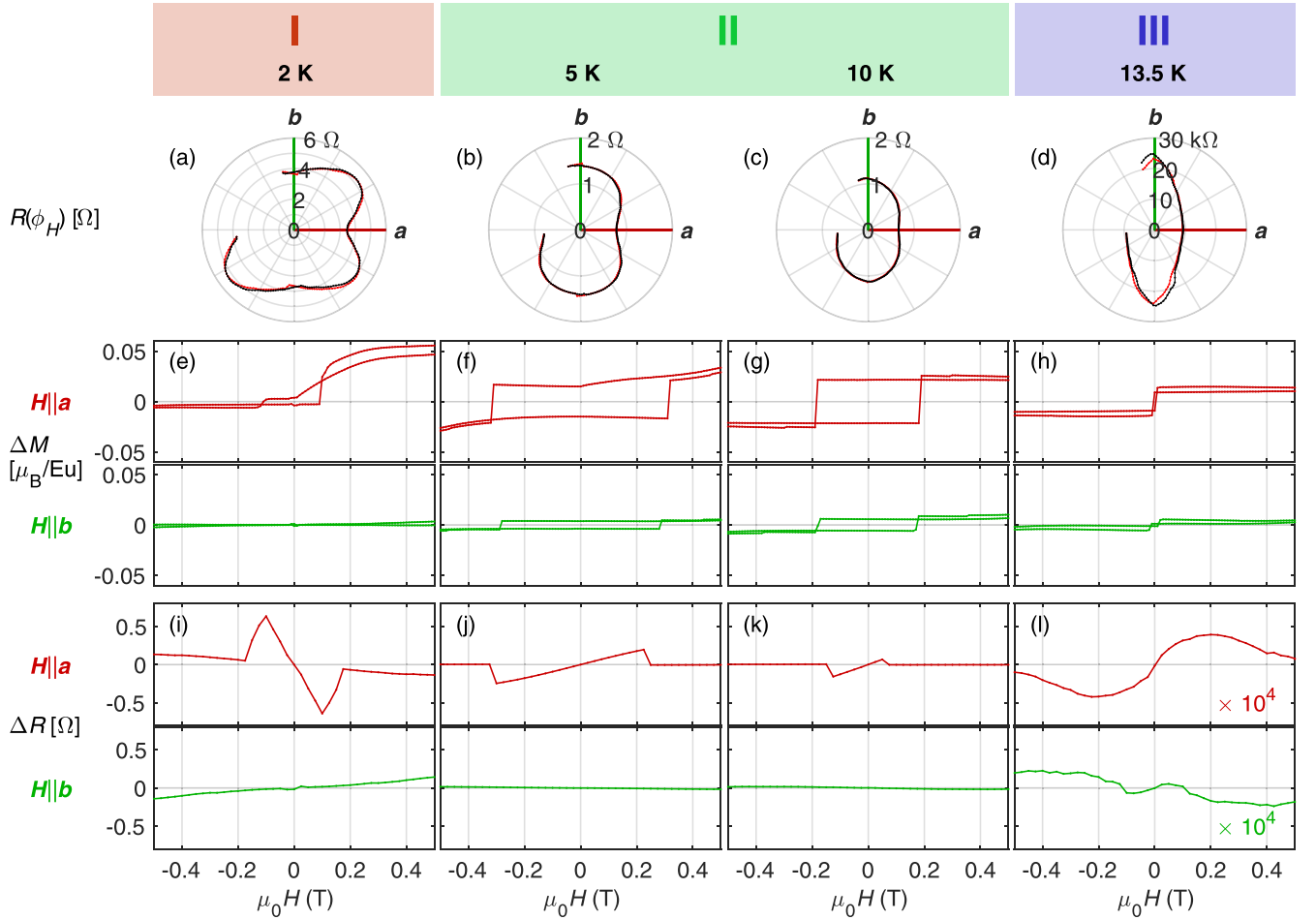


FIG. 6. Characteristic anisotropic hysteretic phenomena in the three regimes of charge transport (I, II, III). (a)–(d) Polar plots of the resistance R at 1 T (current $I \parallel \hat{c}$) for varying field directions ϕ_H in the a - b plane. The three regimes differ not only in the magnitude of R [cf. Fig. 4(c)], but also in their anisotropy. (e)–(h) Respective hysteretic components in the magnetization $\Delta M(H)$ for fields along a and b . Linear slopes have been subtracted from each curve. (i)–(l) Corresponding hysteretic contributions $\Delta R(H) = R(H_\uparrow) - R(H_\downarrow)$ to the resistivity. Note both the quantitative and qualitative variation between the regimes. In regime II (3.0 K \sim 10 K), $\Delta R(H)$ has a positive slope and is concomitant with ΔM . It can therefore be associated with the (re)orientation of magnetic domains of the Γ magnetic order.

and double- q scenarios. However, they show that the coupling to charge transport changes qualitatively in the regime where both components coexist.

III. DISCUSSION

Our findings show that the magnetic ordering process in $\text{Eu}_5\text{In}_2\text{Sb}_6$ is shaped by its nonsymmorphic orthorhombic structure and, specifically, by the fact that magnetic ions occupy multiple, nonequivalent Wyckoff sites. A search for rare-earth intermetallics with these characteristics indeed yields several interesting materials with similarly complex magnetism. For instance, the $R_5\text{Ni}_2\text{In}_4$ structural family is also of $Pbam$ symmetry and also features a rare-earth R on two fourfold and one twofold site. In contrast to the 5-2-6 family, since the R ions are here trivalent, a range of rare earths can be substituted. For instance, a similar complex noncollinear magnetism with multiple phase transitions is found for $R = \text{Tm}$ [20], and similar characteristics, including weak ferromagnetism, can also be obtained above 100 K by substituting $R = \text{Dy}$ [21].

Multiple magnetic (re)ordering transitions at zero field are a common observation among these and related orthorhombic rare-earth intermetallics. This may be attributable to the competition between ferromagnetic and antiferromagnetic itinerant magnetic exchange interactions and, specifically, competing ordering tendencies at inequivalent Wyckoff sites. The low symmetry of these arrangements of localized magnetic ions among anisotropic conduction bands makes for potentially very complex scenarios. For instance, the positions of Eu ions in the basal plane of $\text{Eu}_5\text{In}_2\text{Sb}_6$ can be viewed as a network of distorted corner-sharing or side-sharing triangles, with 6+1 (in-plane + out-of-plane) distinct nearest-neighbor distances ranging between 3.8 Å and 4.7 Å [13]. The layer spacing, 4.6 Å, is intermediate to these values, which emphasizes that competition between in-plane and out-of-plane itinerant exchange is likely, and magnetic correlations are not necessarily two-dimensional. Measurements of the magnetic dynamics in these materials would be of great interest to clarify the hierarchy of correlations.

The small Ising-like net magnetization of the Γ -type magnetic component is a central finding with important

consequences. While dipolar interactions are unlikely a driving force of the magnetic reordering at T_Z , the net magnetization must necessarily lift degeneracies of the electronic structure, which was previously not taken into account in density functional calculations [9,12]. The hysteretic effects imply that magnetic domains play an important role in $\text{Eu}_5\text{In}_2\text{Sb}_6$, that the domain structure is coupled to charge transport, and that this relation changes qualitatively with temperature. Mesoscale transport studies would now be of interest to clarify whether these observations arise from intrinsic variations of the transport channels or extrinsic mechanisms (scattering of charge carriers from domain walls).

The magnetic phase transition at T_Z is driven by a competition of ferro- and antiferromagnetic coupling along the c axis. The two possible scenarios, phase-separation or double- q magnetic order, impose different constraints on the spin arrangement but overall have a similar number of degrees of freedom. Since both models are compatible with magnetic scattering, local and bulk magnetic probes [13], their distinction will require direct evidence from spatially resolved techniques. Notably, both possibilities are unusual results: The double- q structure mixes distinct commensurate structures with different ratios at the three Eu sublattices but only provides a physical solution if these components are strictly orthogonal. The concept of phase separation, as illustrated in Figs. 5(a) and 5(b) is more straightforward, but it is unclear what microscopic mechanism in $\text{Eu}_5\text{In}_2\text{Sb}_6$ could favor inhomogeneity.

IV. CONCLUSION

In this study of the magnetism of the nonsymmorphic Zintl phase $\text{Eu}_5\text{In}_2\text{Sb}_6$, a combination of local, bulk, and momentum-resolved probes of magnetism allowed us to reveal an unusual magnetic ordering process that is also consistent with hysteretic phenomena in both magnetization and charge transport. This complexity originates in the combination of perpendicular glide symmetries and the distribution of localized magnetic moments on three magnetic sublattices. As a consequence, a complex arrangement of ten coplanar Eu spins is endowed with a net magnetic moment along the a axis, which makes each layer an Ising weak ferromagnet. The demagnetization energy therefore takes a decisive role in the bulk magnetism, and a complex behavior of net magnetized domains may be expected on the mesoscale. At lower temperatures, competing interlayer exchange couplings induce a compensated antiferromagnetic component that displaces the weak ferromagnetism. In the absence of microscopic evidence, it is not possible to distinguish whether this transition occurs in the form of a double- q structure or phase separation.

It will be of great interest to clarify what bearing the observed magnetic symmetries have on various proposals for crystalline topological phases in the 5-2-6 Zintls [6,12]. For instance, phase separation would imply the presence of Z -type magnetic regimes that conserve effective time-reversal symmetry (time reversal and translation along c), a prerequisite for the axion insulator state. In either case, the net magnetization of the (variable) Γ components will necessarily have an impact on the valence bands and might also serve

as an unexpected, adjustable (by domain size) parameter of the electronic structure. Furthermore, 5-2-6 Zintls have also been noted for their chemical tunability, and density functional studies predict that the putative topological features in their band structure are extremely sensitive to hydrostatic and uniaxial pressure [12]. Among the wider family of nonsymmorphic orthorhombic intermetallics, there are several structural families in which bulk probes point to similar complex ordering scenarios. Among these are compounds with trivalent rare-earth sites that provide similar potential for non-trivial band topology [22] but open additional possibilities to tune magnetism. Combining the technological potential of weakly ferromagnetic domains and band topology in such materials is an exciting avenue to manipulate topological transport and thus to realize specific technological proposals from the emerging field of topological antiferromagnetic spintronics [23–25].

Note added. Recently, we became aware of a single-crystal neutron diffraction study by Morano *et al.* [26]. Although the data sets are complementary (in terms of the techniques used and the regime of reciprocal space probed), the type of magnetic structures inferred are consistent with our findings. As in our case, the refinement of the single crystal neutron scattering intensities does not allow a clear distinction between the phase separation and double- q models of the Z magnetic component. However, Morano *et al.* observed additional Γ -type magnetic Bragg intensities with qualitatively different temperature dependencies. This implies that the three Eu sublattices already have different ordering tendencies below T_N —which adds to the plausibility of the double- q scenario. On the other hand, density functional calculations by Morano *et al.* appear to favor phase separation.

V. METHODS

A. Samples

Single crystals of $\text{Eu}_5\text{In}_2\text{Sb}_6$ were prepared using an In-Sb flux method, as previously described [9]. This growth technique yields prismatic rods of $\text{Eu}_5\text{In}_2\text{Sb}_6$ (approximately $1 \times 0.5 \times 0.2 \text{ mm}^3$), along with thinner needles, which we identified as the $\text{Eu}_{11}\text{InSb}_9$ phase [27]. To obtain a high-quality powder sample (0.55 g overall), clean $\text{Eu}_5\text{In}_2\text{Sb}_6$ crystals were selected from a large number of batches, cleaned, and ground.

B. Neutron powder diffraction

Time-of-flight neutron powder diffraction was performed at WISH (ISIS, Rutherford Appleton Laboratory) [28], which provides strong signal-to-noise ratio down to very small momentum transfers. This was essential to reveal the magnetic scattering from $\text{Eu}_5\text{In}_2\text{Sb}_6$, given the extreme neutron absorption cross section of Eu, as well as In. To minimize absorption, the sample (0.55 g) was filled into a double-walled vanadium can and cooled in a ^4He cryostat (Oxford Instruments). Data was obtained at 1.5 K, 10.0 K, and 25.0 K, and was processed using MANTID [29] and FULLPROF [30].

C. Muon-spin relaxation

Zero field μ SR studies of polycrystalline samples were performed on the EMU spectrometer at the STFC-ISIS Neutron and Muon Source (pulsed source, higher sensitivity to slow relaxation processes), and the GPS spectrometer at the Swiss Muon Source, Paul Scherrer Institut (continuous source, higher time resolution to resolve static magnetism). Measurements on GPS were performed with the muon spin initially rotated 45° from the incident beam direction and made use of a veto detector to remove the signal from muons that missed the sample. Measurements on EMU were performed with the muon spin antiparallel to the incident beam direction. For the EMU measurements, the sample was mounted on a thick silver plate that stops all muons that miss the sample, yielding a nonrelaxing background signal.

D. Resonant elastic x-ray scattering

Due to the large Eu^{2+} ordered magnetic moment and the strong resonant enhancement at the Eu L absorption edges, hard x-ray resonant elastic scattering (REXS) is highly suitable for magnetic structure determination in Eu compounds. REXS studies were performed at the instruments I16 (Diamond Light Source, Rutherford Appleton Laboratory) [31] and P09 (DESY, Hamburg) [32]. In both cases, the photon energy was tuned to the Eu L_3 ($2p_{3/2} \leftrightarrow 5d$) absorption edge (6.970 keV, $\lambda = 1.779 \text{ \AA}$). Scattered x rays were detected either by a position-sensitive CMOS detector (DECTRIS) or an avalanche photodiode in combination with a Cu (220) analyzer crystal. The orientation of the magnetic structure factor vector $\hat{M}(Q)$ was characterized either by azimuthal scans (I16) or by full linear polarization analysis (P09) [33].

E. Magnetometry and transport measurements

Temperature-dependent magnetic susceptibility and magnetization measurements were performed in a Quantum Design MPMS3 magnetometer. Resistivity measurements were performed in a Quantum Design PPMS using the standard four-point technique and an ac resistance bridge (Lakeshore 372 with 3708 preamp). The current was applied

parallel to the c axis. For the rotation experiments, the sample was mounted on a motor-driven rotation stage. The axis of rotation was parallel to the applied current.

ACKNOWLEDGMENTS

The authors thank J. Müller (Goethe-Universität Frankfurt) for useful discussions. Parts of this research were carried out at Diamond Light Source and at the STFC-ISIS Facility, both institutions of the UK Science and Technology Research Council (STFC). Experiments were also performed at $S\mu S$, Paul Scherrer Institut, Switzerland, as well as under beam-times No. I-20190272 and No. I-20210419 at the synchrotron light source PETRA III at DESY, a member of the Helmholtz Association (HGF). The UK effort was supported by the Engineering and Physical Sciences Research Council (EPSRC) Grant No. EP/N032128/1. M.N.W. acknowledges the support of the Natural Sciences and Engineering Research Council of Canada (NSERC). Work at Los Alamos was supported by the U.S. Department of Energy, Office of Basic Energy Sciences, Division of Materials Science and Engineering project Quantum Fluctuations in Narrow-Band Systems. For work performed at the Paul Scherrer Institute, M.J. acknowledges support from the Swiss National Science Foundation (SNSF) (No. 200650). Work at TU Dresden was supported by the Deutsche Forschungsgemeinschaft through the CRC 1143 (Project ID No. 247310070), the Würzburg-Dresden Cluster of Excellence Complexity and Topology on Quantum Matter – ct.qmat (EXC 2147, Project ID No. 390858490), and through the Emmy Noether program of the German Science Foundation (Project No. 501391385). L.S.I.V. was supported by the UK EPSRC Grants No. EP/N027671/1 and No. EP/N034694/1. M.C.R. is grateful for fellowships provided by the Laboratory Directed Research and Development Program at Los Alamos and the Humboldt Foundation. Research data from the UK effort is available via Durham Collections at Ref. [34]. Muon and neutron data collected at STFC-ISIS are available at Refs. [35]. We thank Dr. P. Biswas and Dr. P. Baker for (ISIS) preliminary μ SR measurements carried out at MuSR.

-
- [1] B. Bradlyn, L. Elcoro, J. Cano, M. G. Vergniory, Z. Wang, C. Felser, M. I. Aroyo, and B. A. Bernevig, *Nature (London)* **547**, 298 (2017).
- [2] T. Zhang, Y. Jiang, Z. Song, H. Huang, Y. He, Z. Fang, H. Weng, and C. Fang, *Nature (London)* **566**, 475 (2019).
- [3] M. G. Vergniory, L. Elcoro, C. Felser, N. Regnault, B. A. Bernevig, and Z. Wang, *Nature (London)* **566**, 480 (2019).
- [4] H. Watanabe, H. C. Po, and A. Vishwanath, *Sci. Adv.* **4**, eaat8685 (2018), .
- [5] Y. Xu, L. Elcoro, Z.-D. Song, B. J. Wieder, M. G. Vergniory, N. Regnault, Y. Chen, C. Felser, and B. A. Bernevig, *Nature (London)* **586**, 702 (2020).
- [6] B. J. Wieder, B. Bradlyn, Z. Wang, J. Cano, Y. Kim, H.-S. D. Kim, A. M. Rappe, C. L. Kane, and B. A. Bernevig, *Science* **361**, 246 (2018), .
- [7] S. Chanakian, U. Aydemir, A. Zevkink, Z. M. Gibbs, J.-P. Fleurial, S. Bux, and G. Jeffrey Snyder, *J. Mater. Chem. C* **3**, 10518 (2015).
- [8] W. Lv, C. Yang, J. Lin, X. Hu, K. Guo, X. Yang, J. Luo, and J.-T. Zhao, *J. Alloys Compd.* **726**, 618 (2017).
- [9] P. F. S. Rosa, Y. Xu, M. Rahn, J. Souza, S. Kushwaha, L. Veiga, A. Bombardi, S. Thomas, M. Janoschek, E. D. Bauer, M. Chan, Z. Wang, J. Thompson, N. Harrison, P. Pagliuso, A. Bernevig, and F. Ronning, *npj Quantum Mater.* **5**, 52 (2020).
- [10] J. C. Souza, S. M. Thomas, E. D. Bauer, J. D. Thompson, F. Ronning, P. G. Pagliuso, and P. F. S. Rosa, *Phys. Rev. B* **105**, 035135 (2022).
- [11] S. Ghosh, C. Lane, F. Ronning, E. D. Bauer, J. D. Thompson, J.-X. Zhu, P. F. S. Rosa, and S. M. Thomas, *Phys. Rev. B* **106**, 045110 (2022).

- [12] N. Varnava, T. Berry, T. M. McQueen, and D. Vanderbilt, *Phys. Rev. B* **105**, 235128 (2022).
- [13] See Supplemental Material at <http://link.aps.org/supplemental/10.1103/PhysRevB.109.174404> for (brief description).
- [14] A. Sekine and K. Nomura, *J. Appl. Phys.* **129**, 141101 (2021), .
- [15] B. A. Bernevig, C. Felser, and H. Beidenkopf, *Nature (London)* **603**, 41 (2022).
- [16] T. J. Hicken, S. J. R. Holt, K. J. A. Franke, Z. Hawkhead, A. Štefančič, M. N. Wilson, M. Gomilšek, B. M. Huddart, S. J. Clark, M. R. Lees, F. L. Pratt, S. J. Blundell, G. Balakrishnan, and T. Lancaster, *Phys. Rev. Res.* **2**, 032001(R) (2020).
- [17] K. J. A. Franke, B. M. Huddart, T. J. Hicken, F. Xiao, S. J. Blundell, F. L. Pratt, M. Crisanti, J. A. T. Barker, S. J. Clark, A. c. v. Štefančič, M. C. Hatnean, G. Balakrishnan, and T. Lancaster, *Phys. Rev. B* **98**, 054428 (2018).
- [18] J. Guo, H. Wang, X. Wang, S. Gu, S. Mi, S. Zhu, J. Hu, F. Pang, W. Ji, H.-J. Gao, T. Xia, and Z. Cheng, *J. Phys. Chem. C* **126**, 13884 (2022).
- [19] N. Papanicolaou, *Phys. Rev. B* **51**, 15062 (1995).
- [20] A. Szytuła, S. Baran, D. Kaczorowski, W. Sikora, and A. Hoser, *J. Alloys Compd.* **617**, 149 (2014).
- [21] A. Provino, Y. Mudryk, D. Paudyal, V. Smetana, P. Manfrinetti, V. K. Pecharsky, K. A. Gschneidner, Jr., and J. D. Corbett, *J. Appl. Phys.* **111**, 07E122 (2012), .
- [22] M. G. Vergniory, B. J. Wieder, L. Elcoro, S. S. P. Parkin, C. Felser, B. A. Bernevig, and N. Regnault, *Science* **376**, eabg9094 (2022).
- [23] L. Šmejkal, Y. Mokrousov, B. Yan, and A. H. MacDonald, *Nat. Phys.* **14**, 242 (2018).
- [24] N. Varnava and D. Vanderbilt, *Phys. Rev. B* **98**, 245117 (2018).
- [25] N. Varnava, J. H. Wilson, J. H. Pixley, and D. Vanderbilt, *Nat. Commun.* **12**, 3998 (2021).
- [26] V. C. Morano, J. Gaudet, N. Varnava, T. Berry, T. Halloran, C. J. Lygouras, X. Wang, C. M. Hoffman, G. Xu, J. W. Lynn *et al.*, [arXiv:2311.00622](https://arxiv.org/abs/2311.00622).
- [27] S. S. Fender, S. M. Thomas, F. Ronning, E. D. Bauer, J. D. Thompson, and P. F. S. Rosa, *Phys. Rev. Mater.* **5**, 074603 (2021).
- [28] L. C. Chapon, P. Manuel, P. G. Radaelli, C. Benson, L. Perrott, S. Ansell, N. J. Rhodes, D. Raspino, D. Duxbury, E. Spill, and J. Norris, *Neutron News* **22**, 22 (2011), .
- [29] O. Arnold, J. Bilheux, J. Borreguero, A. Buts, S. Campbell, L. Chapon, M. Doucet, N. Draper, R. Ferraz Leal, M. Gigg, V. Lynch, A. Markvardsen, D. Mikkelsen, R. Mikkelsen, R. Miller, K. Palmen, P. Parker, G. Passos, T. Perring, P. Peterson *et al.*, *Nucl. Instrum. Methods Phys. Res., Sect. A* **764**, 156 (2014).
- [30] J. Rodríguez-Carvajal, *Phys. B: Condens. Matter* **192**, 55 (1993).
- [31] S. P. Collins, A. Bombardi, A. R. Marshall, J. H. Williams, G. Barlow, A. G. Day, M. R. Pearson, R. J. Woolliscroft, R. D. Walton, G. Beutier, and G. Nisbet, *AIP Conf. Proc.* **1234**, 303 (2010).
- [32] J. Stempfer, S. Francoual, D. Reuther, D. K. Shukla, A. Skaugen, H. Schulte-Schrepping, T. Kracht, and H. Franz, *J. Synchrotron Radiat.* **20**, 541 (2013).
- [33] S. Francoual, J. Stempfer, D. Reuther, D. K. Shukla, and A. Skaugen, *J. Phys.: Conf. Ser.* **425**, 132010 (2013).
- [34] DOI:10.15128/r1zp38wc68k.
- [35] DOI:10.5286/ISIS.E.RB2010313 and DOI:10.5286/ISIS.E.RB1920539.